JPhys Energy

PAPER • OPEN ACCESS

Bifacial flexible CIGS thin-film solar cells with nonlinearly graded-bandgap photon-absorbing layers

To cite this article: Faiz Ahmad *et al* 2024 *J. Phys. Energy* **6** 025012

Journal of Physics: Energy

CrossMark

OPEN ACCESS

RECEIVED
1 September 2023

REVISED
31 January 2024

ACCEPTED FOR PUBLICATION
16 February 2024

PUBLISHED
6 March 2024

PAPER

Bifacial flexible CIGS thin-film solar cells with nonlinearly graded-bandgap photon-absorbing layers

Faiz Ahmad[1,*], **Peter B Monk**[2] **and Akhlesh Lakhtakia**[1]

[1] NanoMM–Nanoengineered Metamaterials Group, Department of Engineering Science and Mechanics, Pennsylvania State University, University Park, PA 16802-6812, United States of America

[2] Department of Mathematical Sciences, University of Delaware, Newark, DE 19716, United States of America

[*] Author to whom any correspondence should be addressed.

E-mail: fua26@psu.edu

Keywords: CIGS solar cells, bandgap grading, optoelectronic optimization, bifacial thin-film solar cell, building-integrated photovoltaics

Abstract

The building sector accounts for 36% of energy consumption and 39% of energy-related greenhouse-gas emissions. Integrating bifacial photovoltaic solar cells in buildings could significantly reduce energy consumption and related greenhouse gas emissions. Bifacial solar cells should be flexible, bifacially balanced for electricity production, and perform reasonably well under weak-light conditions. Using rigorous optoelectronic simulation software and the differential evolution algorithm, we optimized symmetric/asymmetric bifacial CIGS solar cells with either (i) homogeneous or (ii) graded-bandgap photon-absorbing layers and a flexible central contact layer of aluminum-doped zinc oxide to harvest light outdoors as well as indoors. Indoor light was modeled as a fraction of the standard sunlight. Also, we computed the weak-light responses of the CIGS solar cells using LED illumination of different light intensities. The optimal bifacial CIGS solar cell with graded-bandgap photon-absorbing layers is predicted to perform with 18%–29% efficiency under 0.01–1.0-Sun illumination; furthermore, efficiencies of 26.08% and 28.30% under weak LED light illumination of 0.0964 mW cm^{-2} and 0.22 mW cm^{-2} intensities, respectively, are predicted.

1. Introduction

The building sector accounts for 36% of energy consumption and 39% of energy-related carbon-dioxide-equivalent emissions [1]. The space requirement for large-scale solar parks and land-acquisition constraints have discouraged the growth of photovoltaic (PV) installations, particularly in urban areas. Even if land is available for a solar park, there may be a negative impact on agriculture and food security, making it imperative to consider alternative scenarios for deploying solar panels. Another issue is access to electricity in remote areas; some 13% of humans still live without electricity and 40% do not have access to clean fuels for cooking [2]. Hence, on-site off-grid energy generation and management are necessary to cut down buildings-related energy consumption and greenhouse-gas emission as well as to provide access to electricity in remote areas.

The integration of PV technology in new buildings continues to progress [3, 4], but the adoption is slow and needs to be expedited. Thin-film solar cells are flexible, lightweight, easy and cheap to manufacture and can fit well for this role [5]. Thin-film solar cells containing a layer of $CuIn_{1-\xi}Ga_{\xi}Se_2$ (CIGS) represent a high-efficiency alternative to crystalline-silicon solar cells used commercially. CIGS can be deposited on different substrates such as glass, metal foils, transparent conducting oxides, and polymers to allow for applications that require lightweight or flexible modules [6]. These characteristics make CIGS thin-film solar cells attractive for bifacial and flexible applications as well [7], especially for the integration of PV electricity production with human habitation [8–12].

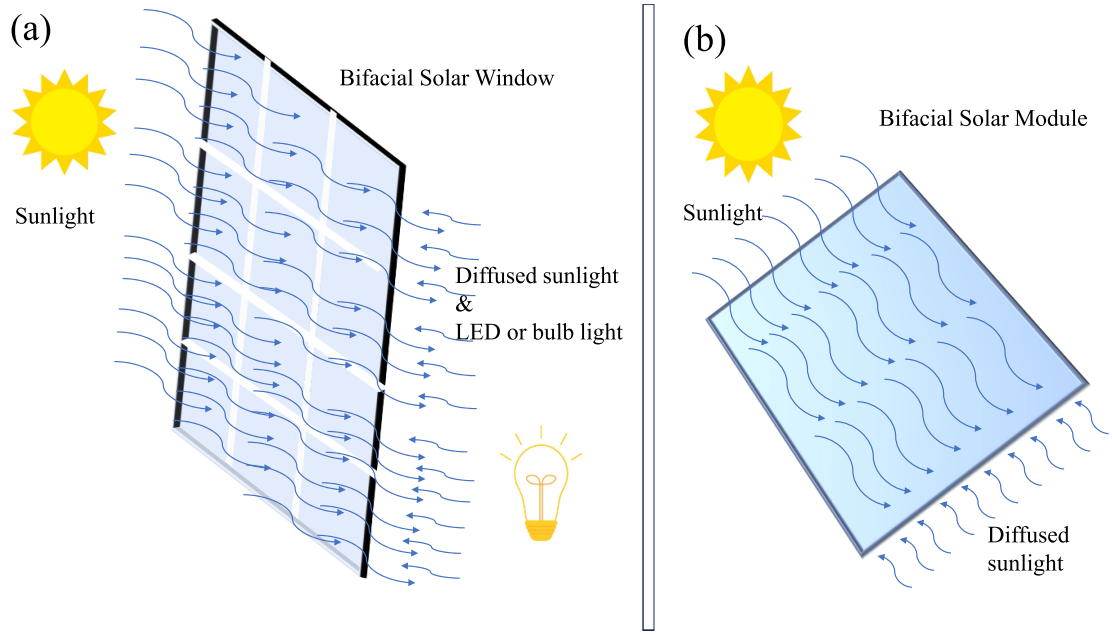

Figure 1. (a) A bifacial solar window comprising solar cells can capture sunlight falling on the front face and diffused daylight or LED light at night falling on the rear face. (b) A bifacial solar module captures direct sunlight falling on the front face and diffused sunlight falling on the rear face.

Flexible solar modules can be straightforwardly installed on rooftops and interior/exterior facades. Bifacial flexible thin-film solar cells will increase the possibility of harnessing energy from direct sunlight, diffused sunlight, as well as indoor light. Also, bifacial thin-film solar cells can capture energy from interior/exterior light at night. Figure 1(a) depicts a bifacial solar cell capturing sunlight falling on the front face and either diffused daylight or LED light at night falling on the rear face. In addition, a bifacial solar module can harvest more energy utilizing both faces of the module by effectively increasing the light capture area, as depicted in figure 1(b).

A standard CIGS solar cell uses a molybdenum (Mo) back-contact layer. In contrast, a bifacial CIGS solar cell has a back-contact layer made of a transparent conducting oxide (TCO) to collect the charge carriers and still remain optically transparent. TCOs include indium-doped tin oxide [10], fluorine-doped tin oxide [11], and aluminum-doped zinc oxide (AZO) [12]. By allowing infrared transmission, a TCO back-contact layer also lowers the solar-cell temperature and thereby increases efficiency [7].

However, in general, all solar cells exhibit lower efficiencies under rear illumination compared to front illumination [11, 13–16]. This is because most charge carriers are generated far from the *p*-*n* junction as the light is absorbed close to the back-contact layer and has difficulty reaching the *p*-*n* junction under rear illumination [15, 16].

The bifaciality factor β, which is the ratio of the efficiency under rear illumination to that under front illumination, must be as close to unity as possible, in order to increase the adoption of bifacial CIGS solar cells for building-integrated and indoor PV applications. One approach is to use two *p*-*n* junctions configured either symmetrically or asymmetrically with a flexible central-contact layer of a TCO, as shown in figure 2(c); see also, the bifacial CZTSSe solar cell of Deng *et al* [17]. Such double-junction bifacial solar cells can be used as either solar windows to capture outdoor light and indoor light simultaneously or solar modules to harvest direct and diffused light simultaneously, as depicted in figure 1. A double-junction bifacial solar cell can be either symmetric or asymmetric, depending upon the optimal design to harvest indoor/outdoor light. Asymmetry of the junctions can be only due to different bandgaps of the two CIGS photon-absorbing layers or different materials for the two junctions. In this study, we consider only the bandgaps of the CIGS photon-absorbing layers to be different, in order to find the optimal configuration for the bifacial design. However, the fabrication of asymmetric double-junction solar cells will be costly compared to their symmetric counterparts. Symmetric bifacial double-junction CIGS solar cells can be fabricated by double-sided deposition techniques to save cost [17]. Furthermore, symmetric bifacial solar modules will have higher lifetimes as either side can be used for direct illumination, and this will decrease the degradation of PV and other materials in the module over time.

A recent theoretical investigation demonstrated that judiciously selected compositional-grading profiles (i.e. ξ as a function of z) leading to bandgap grading [18] in the CIGS photon-absorbing layer can enhance

the efficiency. Furthermore, it has been experimentally observed that, despite the induction of higher defect density by significant compositional grading in the CIGS layer, there is a concurrent reduction in open-circuit voltage loss. This reduction is attributed to enhanced carrier transport at the absorber-buffer interface, facilitated by optimized conduction-band offset [19]. Hence, the incorporation of a graded-bandgap CIGS photon-absorbing layer in bifacial solar cells promises higher efficiency.

In this paper, we report our investigations on bifacial double-junction CIGS solar cells with: (i) two graded-bandgap photon-absorbing layers, one for each junction, and (ii) a flexible AZO central-contact layer. We used a rigorous optoelectronic simulation algorithm, our aim being to arrive at an optimal design to harvest outdoor light and indoor light efficiently. The indoor light was modeled as a fraction of the standard sunlight. Also, we analyzed the weak-light response of the bifacial CIGS solar cell illuminated on the rear face by an 3200 K LED source.

Our theoretical predictions are based on a two-step optoelectronic model [20]. In the optical step of this model, the transfer-matrix method [21, 22] is used to determine the electron–hole-pair (EHP) generation rate G inside the solar cell [18], assuming normal illumination by unpolarized polychromatic light endowed with the AM1.5G solar spectrum [23]. In turn, the EHP generation rate is used in the electrical step as an input to the drift-diffusion system of differential equations to obtain the charge-carrier fluxes and, hence, the current density J_{dev} generated by the solar cell as well as the electrical power density $P = J_{\mathrm{dev}} V_{\mathrm{ext}}$ as functions of the bias voltage V_{ext} under steady-state conditions [18]. In turn, the J_{dev}–V_{ext} and the P–V_{ext} curves yield the efficiency η, short-circuit current density J_{sc}, open-circuit voltage V_{oc}, and fill factor FF [24, 25].

This paper is organized as follows. Section 2 on the optoelectronic simulation of a bifacial thin-film solar cell is divided into three subsections. The description of the solar cell is presented in section 2.1, the optical calculations in section 2.2, and the electrical computations are described in section 2.3. Numerical results on bifacial CIGS thin-film solar cells are discussed in section 3. The paper ends with some remarks in section 4.

2. Optoelectronic simulation

2.1. Solar-cell description

The schematic of a standard MgF_2/AZO/od-ZnO/CdS/CIGS/Al_2O_3/Mo thin-film solar cell is shown in figure 2(a) [18]. The solar cell is homogeneous in any xy plane, the z axis of the Cartesian coordinate system being aligned parallel to the thickness direction. The overall thickness of the solar cell is denoted by L_{t}. On the front face, the 110-nm-thick MgF_2 layer acts as an antireflection coating. Electrons are collected in the 100-nm-thick AZO layer that follows. Then comes an 80-nm-thick layer of oxygen-deficient zinc oxide (od-ZnO) followed by a 70-nm-thick layer of cadmium sulfide (CdS), both materials being n-type semiconductors. The photon-absorbing layer of p-type CIGS is of thickness $L_{\mathrm{s}} \leqslant 2200$ nm, the following 20-nm thick Al_2O_3 layer is needed for passivation, and the 500-nm-thick Mo layer at the rear serves as both the back-contact layer and an optical reflector.

In a simple bifacial CIGS solar cell, the back-contact layer is composed of not Mo but AZO [10–12], as shown in figure 2(b). We kept the thickness of the AZO layer the same as that of the Mo layer it replaces. The bandgap energy was continuously graded in the CIGS layer of the solar cells of figures 2(a) and (b) as [18]

$$\begin{aligned} \mathsf{E}_{\mathrm{g}}(z) &= \mathsf{E}_{\mathrm{g,min}} + A\left(1.626 - \mathsf{E}_{\mathrm{g,min}}\right) \\ &\quad \times \left\{ \frac{1}{2}\left[\sin\left(2\pi K \frac{z - (L_{\mathrm{w}} + L_{\mathrm{od-ZnO}} + L_{\mathrm{CdS}})}{L_{\mathrm{s}}} - 2\pi\psi \right) + 1 \right] \right\}^{\alpha}, \\ &\quad z \in \left[L_{\mathrm{w}} + L_{\mathrm{od-ZnO}} + L_{\mathrm{CdS}}, L_{\mathrm{d}}\right], \end{aligned} \tag{1}$$

where $A \in [0,1]$ is the perturbation amplitude, $\psi \in [0,1]$ quantifies a relative phase shift, K is the number of periods in the CIGS layer, and $\alpha > 0$ is a shaping parameter. The parameter space for optimization of η was fixed as follows: $\mathsf{E}_{\mathrm{g,min}} \in [0.947, 1.626]$ eV, $A \in [0,1]$, $\alpha \in [0,8]$, $K \in [0,8]$, and $\psi \in [0,1]$.

The double-junction bifacial CIGS solar cell with a center-contact layer of AZO is shown in figure 2(c). It is structurally symmetric, in that the thickness of the layer of any material in the front half of the solar cell is the same as the thickness of the layer of the same material in the rear half of the solar cell. When the bandgap energy is also a symmetric function of z, equation (1) is supplemented by the condition

$$\mathsf{E}_{\mathrm{g}}(z) = \mathsf{E}_{\mathrm{g}}(L_{\mathrm{t}} - z), \quad z \in [0, L_{\mathrm{t}}/2]. \tag{2}$$

However, the bandgaps of the two CIGS photon-absorbing layers can be different in asymmetric bifacial solar cells, and equation (2) does not hold for $z \in [L_{\mathrm{w}} + L_{\mathrm{od-ZnO}} + L_{\mathrm{CdS}}, L_{\mathrm{d}}]$.

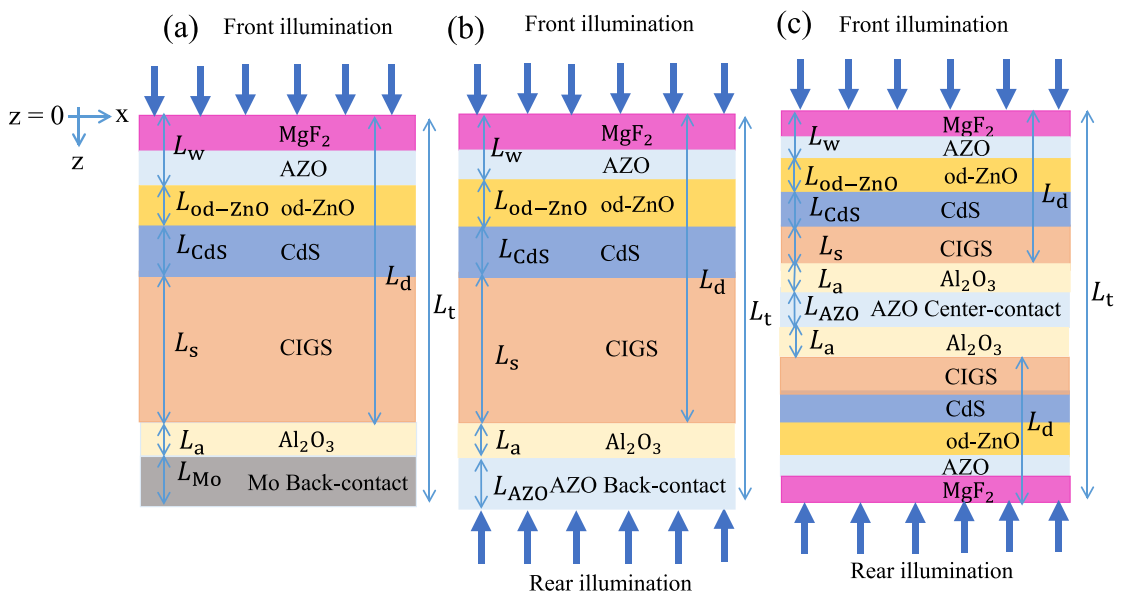

Figure 2. Schematics of three solar cells. (a) CIGS thin-film solar cell with a standard Mo back-contact layer. (b) Bifacial CIGS thin-film solar cell with an AZO back-contact layer. (c) Structurally symmetric bifacial CIGS thin-film solar cell with two *p-n* junctions and an AZO center-contact layer. The layer thicknesses are not proportionally scaled in the schematics.

2.2. Optical calculations

For all three CIGS solar cells shown in figure 2, the transfer-matrix method [21, 26, 27] was used the calculate the electric field phasor $\mathbf{E}(z,\lambda_0) = E_x(z,\lambda_0)\,\hat{\mathbf{u}}_x$ everywhere inside the solar cell as a result of illumination by a monochromatic normally incident plane wave, λ_0 being the free-space wavelength and $\hat{\mathbf{u}}_x$ being the unit vector parallel to the x axis. The electric field phasor of the incident plane wave was taken as

$$\mathbf{E}_{\text{inc}}^{\text{front}}(z,\lambda_0) = E_0\hat{\mathbf{u}}_x \exp\left(i2\pi\frac{z}{\lambda_0}\right) \tag{3}$$

for front illumination, where $E_0 = 4\sqrt{15\pi}$ V m^{-1}. The electric field phasor of the incident plane wave was taken as

$$\mathbf{E}_{\text{inc}}^{\text{rear}}(z,\lambda_0) = E_0\hat{\mathbf{u}}_x \exp\left[-i2\pi\frac{(z-L_t)}{\lambda_0}\right] \tag{4}$$

for rear illumination.

All materials in the solar cell are isotropic dielectric described by the relative permittivity scalar $\varepsilon_{rel}(\lambda_0)$. Spectrums of the real and imaginary parts of $\varepsilon(\lambda_0)/\varepsilon_0$ of MgF_2 [28], AZO [29], od-ZnO [30], CdS [31], CIGS [32, 33], Al_2O_3 [34], and Mo [35] used in our calculations are available in reference [20]. Also, all layers, except the CIGS layer(s) when $A \neq 0$ in equation (1), are homogeneous.

Standard electromagnetic boundary conditions were enforced on the planes $z = 0$ and $z = L_t$ to match the internal field phasors to the incident, reflected, and transmitted field phasors, as appropriate. The procedure to compute the electric field phasor $\mathbf{E}(z,\lambda_0)$ inside the solar cell is the same for both front illumination and rear illumination.

With the assumption that every absorbed photon excites an EHP, the EHP generation rate was calculated as

$$G(z) = \frac{Z_0\varepsilon_0}{\hbar E_0^2}\int_{\lambda_{0,\min}}^{\lambda_{0,\max}(z)} \text{Im}\{\varepsilon_{rel}(z,\lambda_0)\}\,|E_x(z,\lambda_0)|^2\,S(\lambda_0)\,d\lambda_0 \tag{5}$$

in the semiconductor layers. Here, Z_0 is the intrinsic impedance of free space, $\hbar$ is the reduced Planck constant, $S(\lambda_0)$ is the AM1.5G solar spectrum [23], $\lambda_{0,\min} = 300$ nm, and $\lambda_{0,\max}(z) = [1240/\text{E}_g(z)]$ eV nm. Note that $G(z)$ is a piecewise continuous function of z.

2.3. Electrical calculations

EHP generation can occur only in the od-ZnO/CdS/CIGS region of the solar cells shown in figures 2(a) and (b). With Al_2O_3 not being a semiconductor so that $G(z) \equiv 0$ in that layer, electrical calculations have to be

confined to the od-ZnO/CdS/CIGS/Al_2O_3 region bounded by two electrical contact layers. We ignored the 20-nm-thick Al_2O_3 layer and set $L_a = 0$, when we solved a system of 1D drift-diffusion equations [18, 24, 25, 36] to calculate the electron current density $J_n(z)$, the hole current density $J_p(z)$, and the device current density $J_{dev} = J_n(z) + J_p(z), z \in [L_w, L_d]$, which is independent of z but is a function of the voltage V_{ext} applied across the planes $z = L_w$ and $z = L_d$. V_{ext} was varied to determine the maximum value of the electrical power density $P = J_{dev} V_{ext}$ and, hence, the efficiency η.

In a bifacial solar cell of figure 2(c), the central-contact layer functions in the same way for both od-ZnO/CdS/CIGS/Al_2O_3 regions [17] and under either illumination condition. Each of the two od-ZnO/CdS/ CIGS/Al_2O_3 regions is electrically independent, and the electrical power density can be calculated separately for both regions.

3. Numerical results and discussion

3.1. CIGS solar cell with AZO back-contact layer

3.1.1. Homogeneous photon-absorbing layer

Let us begin with a CIGS thin-film solar cell with a Mo back-contact layer and a homogeneous photon-absorbing layer. Values of J_{sc}, V_{oc}, FF, and η predicted by the two-step optoelectronic model for the optimal solar cell for $L_s \in \{1200, 2200\}$ nm are shown in table 1. The highest efficiency predicted is 18.39% for a solar cell with an optimal bandgap of $\mathsf{E}_g = 1.19$ eV [i.e. $\xi \equiv$ Ga/(Ga+In) $= 0.36$]. The corresponding values of J_{sc}, V_{oc}, and FF are 31.86 mA cm^{-2}, 700 mV, and 82.5%, respectively [18]. The best commercial CIGS solar cells today have an efficiency of 19.3% [7]. The disparities between model predictions and experimental data are likely a result of differences in the values of the optical and electrical parameters gleaned from the literature to run our model compared to those of the materials in the practical implementations, but the latter are either partially or wholly unavailable to us [18].

We calculated the performance parameters of CIGS thin-film solar cells with an AZO back-contact layer and a homogeneous photon-absorbing layer under the front illumination of one Sun. Values of J_{sc}, V_{oc}, FF, and η corresponding to the optimal design for $L_s \in \{1200, 2200\}$ nm are shown in table 2. The highest efficiency predicted is 18.27% for a solar cell with an optimal bandgap of $\mathsf{E}_g = 1.19$ eV. The corresponding values of J_{sc}, V_{oc}, and FF are 31.56 mA cm^{-2}, 700 mV, and 83%, respectively. The overall performance of the solar cell, thus, is barely affected by replacing Mo by AZO, as can be noted by comparing tables 1 and 2.

We conjectured that this is because of minimal light transmission to the rear side, as the CIGS layer captures almost all of the light in the relevant spectral regime. To prove the conjecture, we computed the reflectance and transmittance of the front-illuminated CIGS solar cell with either a Mo or an AZO back-contact layer. Figure 3 shows that the transmittance is negligible small for $\lambda_0 \in [300, 1042]$ nm, confirming that almost all of the solar radiation for $\lambda_0 \leqslant 1042$ nm is absorbed within the CIGS photon-absorbing layer. The cutoff wavelength corresponding to $\mathsf{E}_{g,min} = 1.19$ eV is 1042 nm, and it can be noted that the transmission is almost zero below this cutoff wavelength; consequently, there is minimal effect of replacing Mo by AZO. Infrared transmission for $\lambda_0 > 1042$ nm with AZO back-contact layer is due to material transparency [37], and lowers the solar-cell temperature [7].

Next, we calculated the performance parameters of the same solar cell under one-Sun rear illumination. Values of J_{sc}, V_{oc}, FF, and η corresponding to the optimal design for $L_s \in \{1200, 2200\}$ nm are shown in table 2. The highest efficiency predicted for $L_s = 2200$ nm is only 0.55% for a solar cell with an optimal bandgap of $\mathsf{E}_g = 1.19$ eV. The corresponding values of J_{sc}, V_{oc}, and FF are 1.15 mA cm^{-2}, 612 mV, and 78%, respectively.

The bifaciality factor $\beta = 3\%$ is thus very low for this type of solar cell. The rear-illumination efficiency is feeble compared to the front-illumination efficiency, because the majority of the charge carriers are generated far from the *p-n* junction: light is absorbed close to the back-contact layer and thus is highly attenuated near the junction under rear illumination [15, 16].

In order to verify this conjuncture, we analyzed the EHP generation rate $G(z)$ and the EHP recombination rate $R(z)$ under front and rear illumination of the CIGS solar cell with $L_s = 2200$ nm. These rates are plotted in figure 4 as functions of z in the semiconductor region. The EHP generation rate is lower/higher near the back face but higher/lower near the front face, for front/rear illumination.

Furthermore, not only is the cumulative EHP generation rate

$$\gamma = \int_{L_w}^{L_d} G(z)\, dz \tag{6}$$

2.53 times higher for front illumination compared to rear illumination, even the net cumulative EHP generation rate

Table 1. Predicted parameters of the optimal CIGS solar cell with Mo back-contact layer for $L_s \in \{1200, 2200\}$ nm under one-Sun front-illumination condition, when the CIGS layer is homogeneous ($A = 0$, $E_{g,min} \in [0.947, 1.626]$ eV).

L_s (nm)	$E_{g,min}$ (eV)	J_{sc} (mA cm^{-2})	V_{oc} (mV)	FF (%)	η (%)
1200	1.25	28.43	730	81	16.96
2200	1.19	31.86	700	82.5	18.39

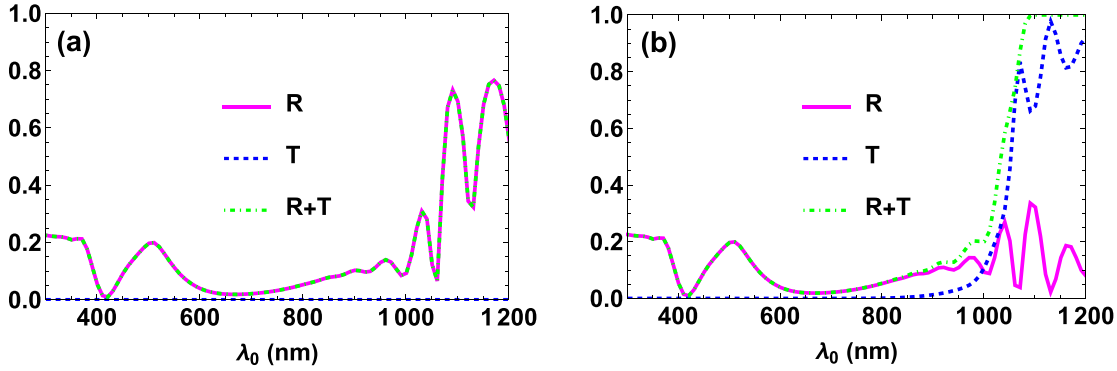

Figure 3. Reflectance R, transmittance T, and the sum R + T of a front-illuminated optimal CIGS solar cell with either (a) a Mo or (b) an AZO back-contact layer, when the 2200-nm-thick CIGS layer is homogeneous.

Table 2. Predicted parameters of the optimal CIGS solar cell with AZO back-contact layer for $L_s \in \{1200, 2200\}$ nm under one-Sun front- and rear-illumination conditions, when the CIGS layer is homogeneous ($A = 0$, $E_{g,min} \in [0.947, 1.626]$ eV).

Illumination	L_s (nm)	$E_{g,min}$ (eV)	J_{sc} (mA cm^{-2})	V_{oc} (mV)	FF (%)	η (%)
Front	1200	1.25	28.19	740	81	16.83
	2200	1.19	31.56	700	83	18.27
Rear	1200	1.25	2.23	670	74	1.09
	2200	1.19	1.15	612	78	0.55

$$\gamma_{net} = \gamma - \rho \tag{7}$$

is 2.47 times higher for front illumination compared to rear illumination, where

$$\rho = \int_{L_w}^{L_d} R(z)\, dz \tag{8}$$

is the cumulative EHP recombination rate. Since the EHP generation rate is higher/lower near the *p-n* junction, for front/rear illumination, the ratio of the front-illumination efficiency to the rear-illumination efficiency is much higher than 2.5. The asymmetry in EHP generation rates for front- and rear-illumination conditions can be attributed to the solar-cell structure. In the case of front illumination, photons must travel through the MgF_2, AZO, od-ZnO, and CdS layers before reaching the CIGS photon-absorbing layer. In contrast, for rear illumination, photons must travel through the AZO and Al_2O_3 layers to reach the CIGS photon-absorbing layer.

According to tables 1 and 2, the efficiency improves by 1.44% for front illumination when the thickness of the CIGS layer increases from 1200 nm to 2200 nm, whether the back-contact layer is made of Mo or AZO. However, for rear illumination (possible with AZO back-contact layer only), the efficiency actually halves when L_s increases from 1200 nm to 2200 nm. Again, this efficiency drop supports the conjecture that light is absorbed close to the back-contact layer and thus is highly attenuated near the junction under rear illumination.

3.1.2. Nonlinearly graded-bandgap photon-absorbing layer

We next considered the performance of a CIGS solar cell with a Mo back-contact layer and a CIGS photon-absorbing layer whose bandgap energy is graded according to equation (1). Values of J_{sc}, V_{oc}, FF, and η corresponding to the optimal design for $L_s \in \{1200, 2200\}$ nm are shown in table 3 [18].

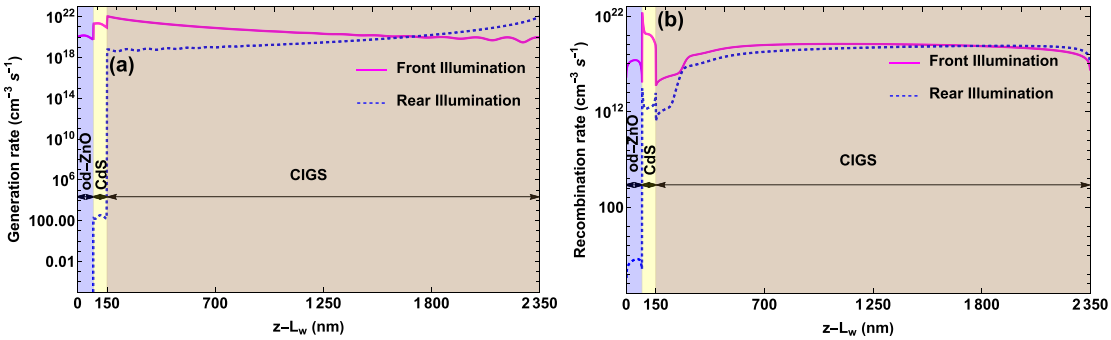

Figure 4. Spatial profiles of (a) the EHP generation rate and (b) the EHP recombination rate in the semiconductor region of the optimal solar cell with a homogeneous CIGS layer of 2200 nm thickness, under one-Sun front- and rear-illumination conditions.

Table 3. Predicted parameters of the optimal CIGS solar cell with Mo back-contact layer for $L_s \in \{1200, 2200\}$ nm under one-Sun front-illumination condition, when the CIGS layer is nonlinearly graded according to equation (1).

L_s (nm)	$E_{g,min}$ (eV)	A	α	K	ψ	J_{sc} (mA cm^{-2})	V_{oc} (mV)	FF (%)	η (%)
1200	1.07	1	8	0.6	0.36	36.36	1000	82	29.74
2200	1.07	1	8	0.6	0.36	38.02	980	80	29.98

Table 4. Predicted parameters of the optimal CIGS solar cell with AZO back-contact layer for $L_s \in \{1200, 2200\}$ nm under one-Sun front- and rear-illumination conditions, when the CIGS layer is nonlinearly graded according to equation (1).

Illumination	L_s (nm)	$E_{g,min}$ (eV)	A	α	K	ψ	J_{sc} (mA cm^{-2})	V_{oc} (mV)	FF (%)	η (%)
Front	1200	1.07	1	8	0.6	0.36	35.23	999	82	28.76
	2200	1.07	1	8	0.6	0.36	37.66	986	80	29.64
Rear	1200	1.07	1	8	0.6	0.36	0.44	510	0.09	0.02
	2200	1.07	1	8	0.6	0.36	0.33	510	0.06	0.01

The predicted efficiency is 29.98% for the 2200-nm-thick CIGS photon-absorbing layer. The corresponding values of J_{sc}, V_{oc}, and FF are 38.02 mA cm^{-2}, 980 mV, and 80%, respectively. The optimal bandgap-energy parameters are as follows: $E_{g,min} = 1.07$ eV, $A = 1$, $\alpha = 8$, $K = 0.6$, and $\psi = 0.36$ [18]. The optimal shaping parameter was identified as the maximum permissible value; hence, we examined values of η for $\alpha > 8$ and determined that $\alpha = 8$ provides optimal results. The efficiency is only 0.14% less for $L_s = 1200$ nm, indicating that the thickness of the CIGS layer can be halved from its industrial value of 2200 nm with insignificant reduction of efficiency, when the CIGS layer is optimally nonhomogeneous.

When Mo is replaced by AZO as the back-contact material, a comparison of tables 3 and 4 indicates a reduction in efficiency under the front-illumination condition. This reduction is 0.98% for $L_s = 1200$ nm but only 0.34% for $L_s = 2200$ nm. Concomitantly, the Mo→AZO replacement has a weak effect on J_{sc}, V_{oc} and FF for both values of L_s.

For additional confirmation, we computed the reflectance and transmittance of the front-illuminated CIGS solar cell with either a Mo or an AZO back-contact layer. Figure 5 shows that the transmittance is negligible small for $\lambda_0 \in [300, 900]$ nm and confirming that almost all of the solar radiation for $\lambda_0 \leqslant 900$ nm is absorbed within the CIGS photon-absorbing layer. Since the AM1.5G solar spectrum is considerably weaker in the near-infrared spectral regime than in the visible spectral regime, the Mo→AZO replacement has a weak effect on the solar-cell performance.

Finally, for the optimal rear-illuminated solar cell with a nonlinearly graded-bandgap CIGS layer of thickness $L_s \in \{1200, 2200\}$ nm and an AZO back-contact layer, the predicted values of J_{sc}, V_{oc}, FF, and η are shown in table 4. The rear-illumination efficiency is poor, and that is because the majority of the charge carriers are generated far from the *p-n* junction as light is absorbed close to the back-contact layer [15, 16]. Plots of $G(z)$ vs. z in figure 6 for $L_s = 2200$ nm provide confirmation.

The rear-illumination efficiency of the solar cell with a nonlinearly graded-bandgap CIGS layer is inferior to the rear-illumination efficiency of the solar cell containing a homogeneous-bandgap CIGS layer. This discrepancy primarily stems from a reduced current density associated with the nonlinearly graded-bandgap

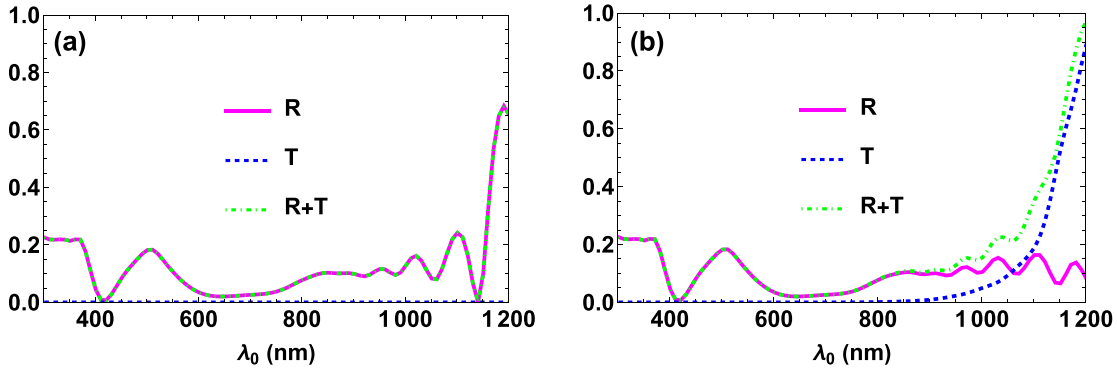

Figure 5. Reflectance R, transmittance T, and the sum R + T of a front-illuminated optimal CIGS solar cell with either (a) a Mo or (b) an AZO back-contact layer, when the 2200-nm-thick CIGS layer is nonlinearly graded according to equation (1).

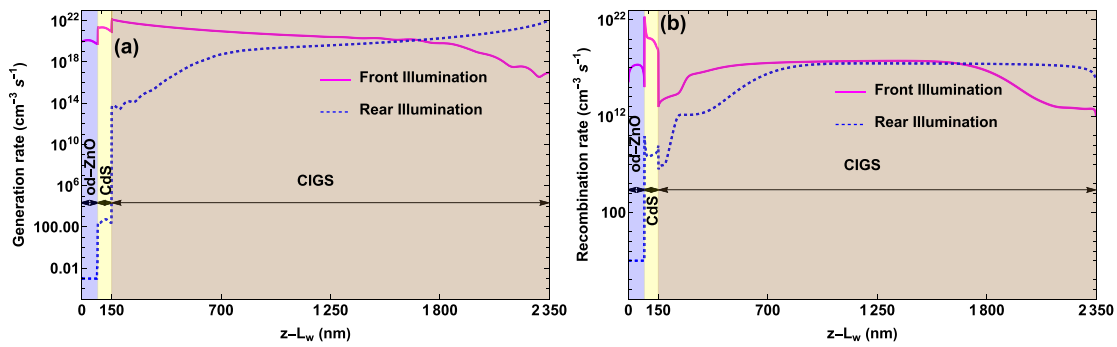

Figure 6. Spatial profiles of (a) the EHP generation rate and (b) the EHP recombination rate in the semiconductor region of the optimal solar cell with a nonlinearly graded-bandgap CIGS layer of 2200 nm thickness, under one-Sun front- and rear-illumination conditions.

CIGS layer. It is crucial to highlight that optimizing the nonlinearly graded-bandgap CIGS layer for front illumination does not guarantee optimal performance for rear illumination.

3.2. Structurally symmetric bifacial solar cell with AZO center-contact layer

An approach to solving the problem of poor performance of bifacial thin-film solar cells under front/rear illumination is using the double-junction format with a center-contact layer, as shown in figure 2(c). The efficiencies of the bifacial symmetric double-junction solar cell remain the same under the front- and rear-illumination conditions with the same sunlight intensity (i.e. $\beta = 100\%$), because the central-contact layer is sufficiently thick (500 nm) to decouple the two *p-n* junctions. The optical decoupling is expected from the low rear-illumination efficiencies reported in tables 2 and 4 for the solar cell shown in figure 2(b). The electrical decoupling follows from the high d.c. conductivity of the material of the center-contact layer.

However, performance under diffused light needs to be considered for rear-illumination conditions to be encountered for the applications illustrated in figure 1. Hence, we replaced $S(\lambda_0)$ by $c_{\mathrm{Sun}}S(\lambda_0)$, $c_{\mathrm{Sun}} \in [0.01, 1]$, in the optoelectronic model to analyze the performance of a bifacial solar cell in relation to the sunlight-concentration factor c_{Sun}. Solar cells with both photon-absorbing layers either homogeneous or nonlinearly graded were considered.

A structurally symmetric bifacial solar cell can be considered as two identical solar cells cascaded back-to-back. Optical calculations were made and $G(z)$ was determined for the entire bifacial solar cell. For electrical calculations, the front and the rear solar cells (each with an electrically isolated od-ZnO/CdS/CIGS/Al_2O_3 region) were considered separately.

3.2.1. Homogeneous photon-absorbing layers

We begin with the case of both photon-absorbing layers being identical and homogeneous ($A = 0$) with $L_s = 2200$ nm. The bandgap energy $E_{g,min}$ was optimized for diverse values of $c_{\mathrm{Sun}} \in [0.01, 1]$. The optimal bandgap energy $E_{g,min}$ ($= 1.19$ eV) was found to be independent of c_{Sun}.

Plots of J_{sc}, V_{oc}, η, FF, and P of the rear solar cell as functions of $c_{\mathrm{Sun}} \in [0.01, 1]$ are shown in figure 7. When $c_{\mathrm{Sun}} = 0.01$, the efficiency predicted is 14.79% with corresponding values of J_{sc}, V_{oc}, and FF being

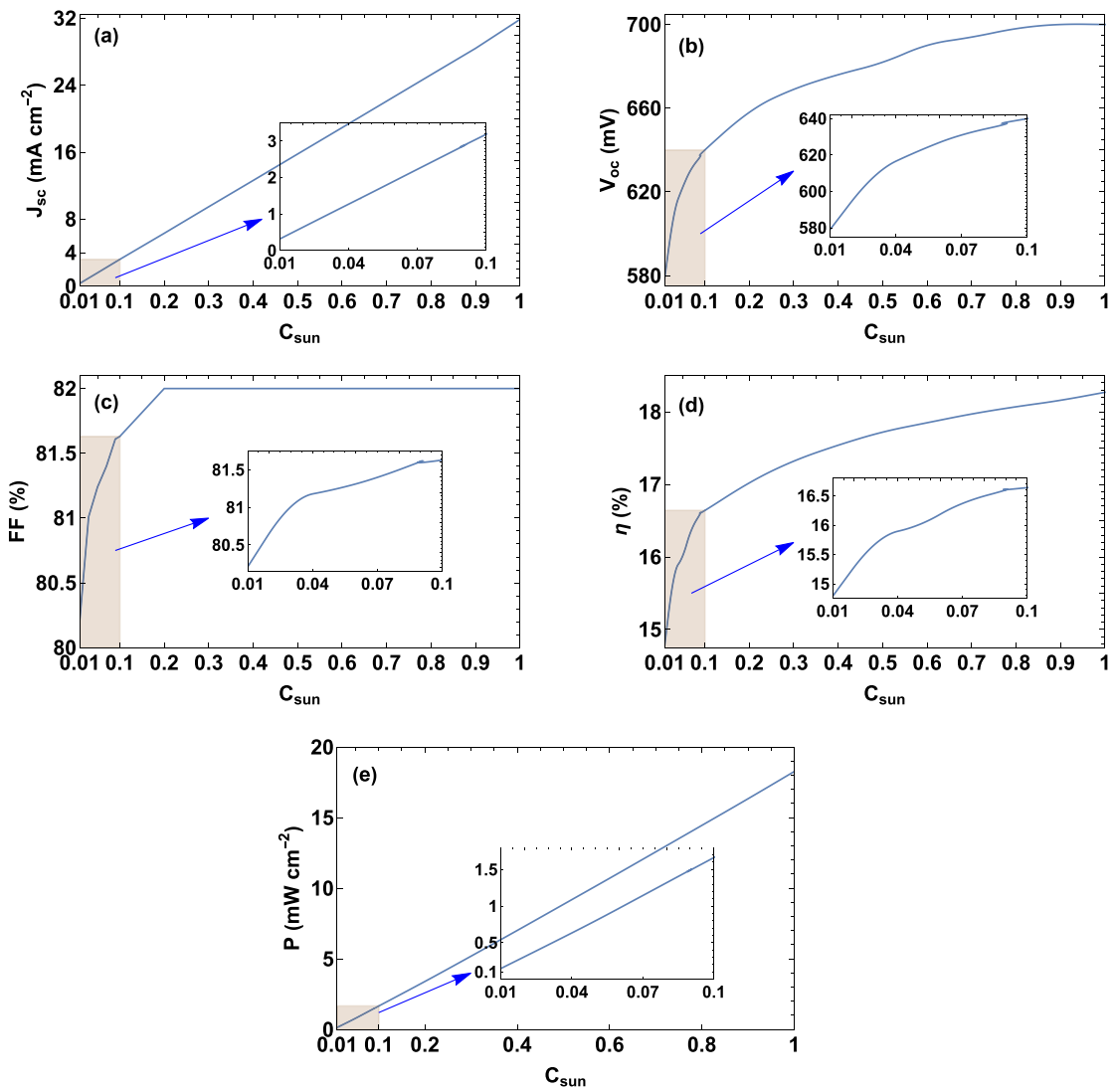

Figure 7. Plots of (a) J_{sc}, (b) V_{oc}, (c) FF, (d) η, and (e) P of the rear solar cell in a structurally symmetric double-junction thin-film solar cell with homogeneous 2200-nm-thick CIGS layer under rear illumination of $c_{Sun} \in [0.01, 1]$.

0.3186 mA cm^{-2}, 579 mV, and 80.21%, respectively. The electrical power density generated by the rear solar cell is 0.1479 mW cm^{-2}. The efficiency rises with increase of c_{Sun} and reaches 18.27% for $c_{Sun} = 1$ with $P = 18.27$ mW cm^{-2}.

The linear relationship of J_{sc} with c_{Sun} is evident in figure 7(a), the underlying reason being that the EHP generation rate is higher when the illumination is more intense. Both dV_{oc}/dc_{Sun} and $d\eta/dc_{Sun}$ in figures 7(b) and (d) decrease continuously with increasing c_{Sun}. Also, FF in figure 7(c) first increases rapidly as c_{Sun} rises and then $d\mathrm{FF}/dc_{Sun}$ reduces rapidly to a negligibly small value. The reason for lower V_{oc} at smaller c_{Sun} is that J_{sc} is lower too and V_{oc} is proportional to $\ln(1 + J_{sc}/J_{dark})$ for ideal photodiodes, where J_{dark} is the dark current density; see equation (1.6) of reference [24].

The front solar cell in the bifacial solar cell generates an additional 0.157 mW cm^{-2} power density under rear illumination with $c_{Sun} = 1$ (which is not possible using a Mo center-contact layer). This power density is high enough for the operation of most internet-of-things (IoT) devices [38].

Each of the two solar cells in the symmetric double-junction CIGS solar cell with the AZO center-contact layer is 14.79% efficient even with one-hundredth of solar radiation. In comparison, a rear-illuminated single-junction CIGS thin-film solar cell with an AZO back-contact layer has an efficiency of only 0.55% (table 2).

3.2.2. Nonlinearly graded-bandgap photon-absorbing layers

Next, we considered the case of both photon-absorbing layers being identical with a nonlinearly graded bandgap energy described by equations (1) and (2) and thickness $L_s = 2200$ nm. We found that the optimal

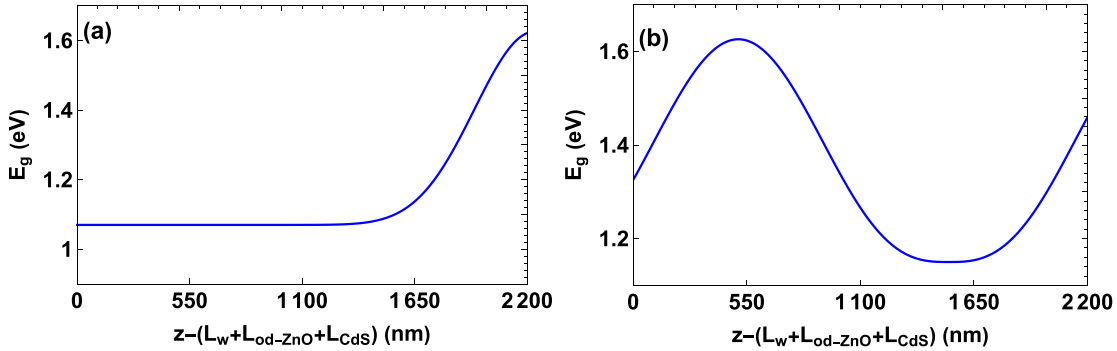

Figure 8. Spatial profile of E_g of (a) a structurally symmetric bifacial solar cell and (b) a structurally asymmetric bifacial solar cell. The 2200-nm-thick photon-absorbing layers are nonlinearly graded in accordance with equation (1).

bandgap-energy parameters $E_{g,min} = 1.07$ eV, $A = 1$, $\alpha = 8$, $K = 0.6$, and $\psi = 0.36$ [18] do not change with $c_{Sun} \in [0.01, 1]$ in the chosen parameter space. The optimal spatial profile of E_g is provided in figure 8(a).

Plots of J_{sc}, V_{oc}, FF, η, and P of the rear solar cell as functions of $c_{Sun} \in [0.01, 1]$ are shown in figure 9. When $c_{Sun} = 0.01$, the efficiency predicted is 18.84% and corresponding values of J_{sc}, V_{oc}, and FF are 0.377 mA cm^{-2}, 641 mV, and 77.91%, respectively. The power density generated by the rear solar cell is 0.1884 mW cm^{-2}. The efficiency increases as c_{Sun} does, reaching 29.26% for $c_{Sun} = 1$ with $P = 29.26$ mW cm^{-2}.

In figure 9(a), J_{sc} increases linearly with $c_{Sun} \in [0.1, 1]$. But the J_{sc}–c_{Sun} relationship is nonlinear for low light intensity ($c_{Sun} < 0.1$), which can be correlated with the injection-dependent bulk and surface recombination rates [39], and inversion layer shunting [40]. Both V_{oc} and η in figures 9(b) and (d), respectively, increase with c_{Sun}, but the rates of increase diminish with increasing c_{Sun}. As explained for figure 7 in section 3.2.1, J_{sc} has to be directly proportional to the illumination intensity and that V_{oc} is proportional to $\ln(1 + J_{sc}/J_{dark})$ for ideal photodiodes. The fill factor in figure 9(c) exhibits a two-phase trend: as the concentration c_{Sun} rises from 0.01 to 0.1, the fill factor initially decreases before increasing. However, in the second phase, the slope decreases consistently with the continued increase in c_{Sun}. A plausible explanation for the dip in fill factor is an elevation in the solar cell's equivalent resistance at that specific illumination intensity, indicative of the solar cell's poor quality [41].

Each of the two solar cells in the structurally symmetric bifacial configuration is 18.84% efficient even when $c_{Sun} = 0.01$. In comparison, a rear-illuminated single-junction CIGS thin-film solar cell with an AZO back-contact layer has an efficiency of a minuscule 0.01% (table 4).

3.3. Structurally asymmetric bifacial solar cell with AZO center-contact layer

We also considered structurally asymmetric bifacial solar cells. Both photon-absorbing layers were taken to be of the same thickness. Both could be homogeneous, or both could have nonlinearly graded bandgap with different sets of bandgap-grading parameters, or one could be homogeneous and the other have nonlinearly graded bandgap. The bandgap-energy parameters of the two photon-absorbing layers were optimized independently for $c_{Sun} \in [0.01, 1]$ under rear-illumination conditions. The optoelectronic model predicted that the structurally symmetric configuration conforming to equation (2) is optimal, as expected from the optoelectronic decoupling characteristics of the AZO center-contact layer. Therefore, all of the results presented in section 3.2 remain valid for structurally asymmetric bifacial solar cells.

3.4. Weak-light LED response

For solar windows, the front solar cell needs to be optimized for the solar spectrum, while the rear solar cell needs to be optimized for the daytime diffused indoor light or nighttime LED light. The rear cell was found to be optimal for the indoor diffused light in sections 3.2 and 3.3 but will be suboptimal for harvesting LED light. However, that suboptimality should be acceptable because optimal daytime generation would greatly surpass optimal nighttime generation.

If only LED light is available during the day and the night, the rear cell must be optimized for LED light rather than for daytime diffused indoor light. The normalized spectrum of 3200 K LED is available for a luminance of 200 lm and 500 lm, with corresponding irradiances of 0.0964 mW cm^{-2} and 0.220 mW cm^{-2}, respectively [42]. Optical calculations have to be made for $\lambda_0 \in [300, 900]$ nm.

For the structurally symmetric solar cells, we used the optimal bandgap-energy parameters predicted for front illumination in section 3.2. The same bandgap-energy parameters were chosen for the front solar cell in

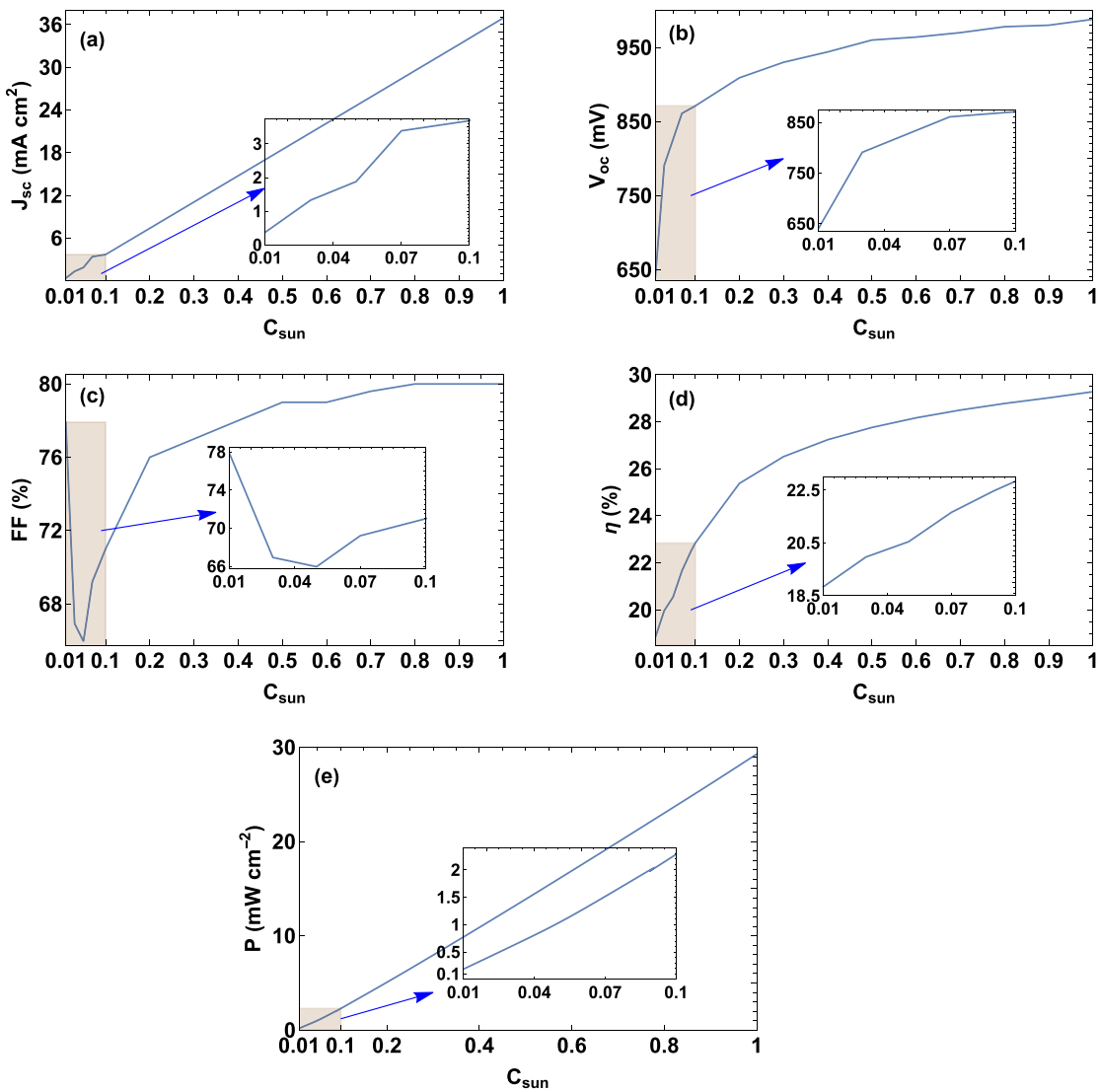

Figure 9. Plots of (a) J_{sc}, (b) V_{oc}, (c) FF, (d) η, and (e) P of the rear solar cell in a structurally symmetric double-junction thin-film solar cell with 2200-nm-thick nonlinearly graded-bandgap CIGS layer under rear illumination of $c_{Sun} \in [0.01, 1]$.

a structurally asymmetric bifacial solar cell, but we optimized the bandgap-energy parameters of the rear solar cell for the illumination by a 3200 K LED.

3.4.1. Structurally symmetric bifacial solar cell with homogeneous photon-absorbing layers
Values of J_{sc}, V_{oc}, FF, and η of the rear solar cell in the optimal design for $L_s \in \{1200, 2200\}$ nm presented in section 3.2 are provided in table 5 for two luminance values: 200 lm and 500 lm.

200 lm luminance. When $L_s = 1200$ nm, the efficiency of the rear solar cell is predicted as 17.59%. The corresponding values of J_{sc}, V_{oc}, and FF are 0.0412 mA cm^{-2}, 549 mV, and 75%, respectively. When $L_s = 2200$ nm, the predicted efficiency is 18.28%, along with $J_{sc} = 0.0428$ mA cm^{-2}, $V_{oc} = 525$ mV, and FF = 78%. The lower short-circuit current densities compared to solar illumination are due to weakness of LEDs as light sources. Thus, the total irradiance intensity of 3200 K LED with a luminance of 200 lm is 0.0964 mW cm^{-2}, which is almost a thousand times lower than the total solar irradiance intensity (100 mW cm^{-2}).

500 lm luminance. When $L_s = 1200$ nm, the predicted efficiency of the rear solar cell is 19.70%, along with $J_{sc} = 0.1062$ mA cm^{-2}, $V_{oc} = 577$ mV, and FF = 76%. When $L_s = 2200$ nm, the efficiency is $\eta = 20.25\%$. The corresponding values of J_{sc}, V_{oc}, and FF are 0.1022 mA cm^{-2}, 549 mV, and 79%, respectively. Efficiency increases with higher luminance, the major reason being that J_{sc} is enhanced as a consequence of the higher EHP generation rate with stronger illumination.

3.4.2. Structurally symmetric bifacial solar cell with nonlinearly graded-bandgap photon-absorbing layers
For the luminance values of 200 lm and 500 lm, table 6 provides values of J_{sc}, V_{oc}, FF, and η of the rear solar cell in the optimal design for $L_s \in \{1200, 2200\}$ nm presented in section 3.2.

Table 5. Predicted parameters of the rear solar cell in the optimal structurally symmetric double-junction solar cell with AZO center-contact layer under rear illumination by a 3200 K LED for $L_s \in \{1200, 2200\}$ nm and two different luminance values, when the CIGS layer is homogeneous. The bandgap-energy parameters are the same as in table 2.

Intensity	L_s (nm)	$E_{g,min}$ (eV)	J_{sc} (mA cm^{-2})	V_{oc} (mV)	FF (%)	η (%)
200 lm	1200	1.25	0.0412	549	75	17.59
	2200	1.19	0.0428	525	78	18.28
500 lm	1200	1.25	0.1062	577	76	19.70
	2200	1.19	0.1022	549	79	20.25

Table 6. Predicted parameters of the rear solar cell in the optimal structurally symmetric double-junction solar cell with AZO center-contact layer under rear illumination by a 3200 K LED for $L_s \in \{1200, 2200\}$ nm and two different luminance values, when the CIGS layer is nonlinearly graded according to equation (1). The bandgap-energy parameters are the same as in table 4.

Intensity	L_s (nm)	$E_{g,min}$ (eV)	A	α	K	ψ	J_{sc} (mA cm^{-2})	V_{oc} (mV)	FF (%)	η (%)
200 lm	1200	1.07	1	8	0.6	0.36	0.0440	569	80	20.86
	2200	1.07	1	8	0.6	0.36	0.0442	552	81	20.29
500 lm	1200	1.07	1	8	0.6	0.36	0.1064	602	80	22.94
	2200	1.07	1	8	0.6	0.36	0.1055	580	81	22.33

Table 7. Predicted parameters of the optimal rear solar cell in the structurally asymmetric double-junction solar cell with AZO center-contact layer under rear illumination by a 3200 K LED for $L_s \in \{1200, 2200\}$ nm and two different luminance values, when the CIGS layer is homogeneous.

Intensity	L_s (nm)	$E_{g,min}$ (eV)	J_{sc} (mA cm^{-2})	V_{oc} (mV)	FF (%)	η (%)
200 lm	1200	1.35	0.0389	605	73	17.74
	2200	1.19	0.0428	525	78	18.28
500 lm	1200	1.35	0.0928	639	74	19.94
	2200	1.19	0.1022	549	79	20.25

The predicted maximum efficiency is 20.86% for 200 lm luminance and 22.94% for 500 lm luminance, when $L_s = 1200$ nm. The predicted maximum efficiency is 20.29% for 200 lm luminance and 22.33% for 500 lm luminance, when $L_s = 2200$ nm. The lower values of the short-circuit current density in table 6 compared to the case of direct one-Sun illumination arise from the lower irradiance intensities of LEDs, as was also noted for solar cells with homogeneous CIGS photon-absorbing layers in section 3.4.1. In conformity, an increase in LED luminance increases J_{sc} and, therefore, η.

3.4.3. Structurally asymmetric bifacial solar cell with homogeneous photon-absorbing layers

Next, optoelectronic optimization was carried out for rear illumination by 3200 K LED of the rear solar cell, the optimal front solar cell being the same as for table 2. Values of J_{sc}, V_{oc}, FF, and η of the optimal rear solar cell for $L_s \in \{1200, 2200\}$ nm are presented in table 7 for 200 lm and 500 lm luminance values.

For 200 lm luminance, the maximum efficiency of the rear solar cell is predicted to be 17.74% for $L_s = 1200$ nm with $E_{g,min} = 1.35$ eV, and 18.28% for $L_s = 2200$ nm with $E_{g,min} = 1.19$ eV. For 500 lm luminance, the maximum efficiency of the rear solar cell is predicted to be 19.94% for $L_s = 1200$ nm with $E_{g,min} = 1.35$ eV and 20.25% for $L_s = 2200$ nm with $E_{g,min} = 1.19$ eV. Efficiency increases with higher luminance, mostly due to enhanced short-circuit current density which is a consequence of higher EHP generation rate with stronger illumination.

3.4.4. Structurally asymmetric bifacial solar cell with nonlinearly graded-bandgap photon-absorbing layers

Values of J_{sc}, V_{oc}, FF, and η corresponding to the optimal design of the rear solar cell for $L_s \in \{1200, 2200\}$ nm are shown in table 8 under rear illumination by 3200 K LED with luminance of either 200 lm or 500 lm.

200 lm luminance. When $L_s = 1200$ nm, the maximum efficiency predicted is 23.22% with $J_{sc} = 0.0426$ mA cm^{-2}, $V_{oc} = 632$ mV, and FF = 83%, respectively. We found that the optimal bandgap-energy parameters $E_{g,min} = 1.16$ eV, $A = 1$, $\alpha = 5.49$, $K = 1.27$, and $\psi = 0.75$. When $L_s = 2200$ nm, the maximum efficiency predicted is 26.08%, and the values of J_{sc}, V_{oc}, and FF are 0.0332 mA cm^{-2}, 895 mV,

Table 8. Predicted parameters of the optimal rear solar cell in the structurally asymmetric double-junction solar cell with AZO center-contact layer under rear illumination by a 3200 K LED for $L_s \in \{1200, 2200\}$ nm and two different luminance values, when the CIGS layer is nonlinearly graded according to equation (1).

Intensity	L_s (nm)	$\mathsf{E}_{g,min}$ (eV)	A	α	K	ψ	J_{sc} (mA cm^{-2})	V_{oc} (mV)	FF (%)	η (%)
200 lm	1200	1.16	1	5.49	1.27	0.75	0.0426	632	83	23.22
	2200	1.15	1	1.44	1.08	0	0.0332	895	85	26.08
500 lm	1200	1.16	1	5.49	1.27	0.75	0.1013	658	83	25.14
	2200	1.15	1	1.44	1.08	0	0.0792	921	85	28.30

and 85%, respectively. The optimal spatial profile of E_g, illustrated in figure 8(b), was computed with $\mathsf{E}_{g,min} = 1.15$ eV, $A = 1$, $\alpha = 1.44$, $K = 1.08$, and $\psi = 0$ [18], and it is different from that the structurally symmetric solar cell with nonlinearly graded-bandgap photon-absorbing layers. Also, the optimal bandgap-energy parameters vary with the illumination intensity of the LED.

500 lm luminance. When $L_s = 1200$ nm, the maximum efficiency predicted is 25.14% with $J_{sc} = 0.1013$ mA cm^{-2}, $V_{oc} = 658$ mV, and FF = 83%, respectively. When $L_s = 2200$ nm, the maximum efficiency predicted is 28.30%, and the values of J_{sc}, V_{oc}, and FF are 0.0792 mA cm^{-2}, 921 mV, and 85%, respectively.

Note that, for fixed L_s, the optimal bandgap-energy parameters do not change with luminance, but are different from their counterparts for solar illumination. These data suggest that solar cells meant to harvest indoor LED light must be designed differently for those meant to harvest outdoor sunlight.

4. Concluding remarks

We optimized structurally symmetric and structurally asymmetric bifacial CIGS solar cells with two graded-bandgap photon-absorbing layers and a flexible AZO center-contact layer to harvest outdoor and indoor light efficiently. In addition, we computed the weak-light response of the solar cells using LED illumination. Definitely, optimal nonlinear grading of bandgap energy elevates the solar-cell efficiency.

The structurally symmetric double-junction CIGS solar cell is suitable for outdoor applications. Solar modules with these solar cells will have higher lifetimes as either side can be used for direct illumination, decreasing the material degradation over time. Also, if only a fraction $c_{Sun} < 1$ of 100 mW cm^{-2} sunlight is received as diffused light on the rear face of the optimal solar cell with nonlinearly graded-bandgap photon-absorbing layers of 2200 nm thickness, it would generate between 0.1884 and 2.284 mW cm^{-2} (depending on the value of $c_{Sun} \in (0.01, 0.1)$) of electrical power, whereas the front solar cell would generate 29.26 mW cm^{-2}.

In the case of solar windows, the indoor diffused sunlight available has to be harvested through the rear face of the bifacial solar cell. Optoelectronic optimization predicts a good efficiency under low diffused light (as low as 1 mW cm^{-2}), with a structurally symmetric bifacial solar cell with nonlinearly graded-bandgap CIGS photon-absorbing layers being the best choice. If the indoor light will always be that from LEDs, the optimal structurally asymmetric bifacial solar cell will perform better than the optimal structurally symmetric bifacial solar cell, as can be seen from comparing tables 6 and 8. We expect that our optimization results will help in cutting a significant portion of energy consumption and related emissions in built environments.

Data availability statement

All data that support the findings of this study are included within the article.

Acknowledgments

The authors appreciate constructive comments from two anonymous reviewers. A Lakhtakia thanks the Charles Godfrey Binder Endowment at The Pennsylvania State University for ongoing support of his research. The research of F Ahmad and A Lakhtakia was partially supported by US National Science Foundation (NSF) under Grant Number DMS-2011996. The research of P B Monk was supported by the US NSF under Grant Number DMS-2011603.

Funding

US National Science Foundation (DMS-2011 996 and DMS-2011 603).

Conflict of interest

The authors declare no conflicts of interest.

ORCID iDs

Faiz Ahmad https://orcid.org/0000-0002-0635-207X
Peter B Monk https://orcid.org/0000-0002-6539-5897
Akhlesh Lakhtakia https://orcid.org/0000-0002-2179-2313

References

[1] Shabunko V, Badrinarayanan S and Pillai D S 2021 Evaluation of *in-situ* thermal transmittance of innovative building integrated photovoltaic modules: application to thermal performance assessment for green mark certification in the tropics *Energy* **235** 121316
[2] Ritchie H, Rosado P and Roser M 2019 *Access to Energy* (Our World in Data) (available at: https://ourworldindata.org/energy-access)
[3] Zhang T, Wang M and Yang H A 2018 Review of the energy performance and life-cycle assessment of building-integrated photovoltaic (BIPV) systems *Energies* **11** 3157
[4] BCC Research 2016 Building-Integrated Photovoltaics (BIPV): technologies and global markets *A BCC Energy and Resources Report* (available at: www.bccresearch.com/market-research/energy-and-resources/building-integrated-photovoltaics-markets-report.html)
[5] Ramanujam J, Bishop D M, Todorov T K, Gunawan O, Rath J, Nekovei R, Artegiani E and Romeo A 2020 Flexible CIGS, CdTe and a-Si:H based thin film solar cells: a review *Prog. Mater. Sci.* **110** 100619
[6] Carron R, Nishiwaki S, Feurer T, Hertwig R, Avancini E, Löckinger J, Yang S-C, Buecheler S and Tiwari A N 2009 Advanced alkali treatments for high-efficiency Cu(In,Ga)Se_2 solar cells on flexible substrates *Adv. Energy Mater.* **9** 1900408
[7] SPIE 2023 First Solar to build 5th US factory (available at: https://optics.org/news/14/8/3?utm_id=znews0823e&spMailingID=9861220&spUserID=NDIwNzA5OTQzMjMS1&spJobID=1800452026&spReportId=MTgwMDQ1MjAyNgS2)
[8] Mazzer M *et al* 2017 Bifacial CIGS solar cells grown by low temperature pulsed electron deposition *Sol. Energy Mater. Sol. Cells* **166** 247–53
[9] Masuda T, Hirai S, Inoue M, Chantana J, Kudo Y and Minemoto T 2018 Colorful, flexible and lightweight Cu(In, Ga)Se_2 solar cell by lift-off process with automotive painting *IEEE J. Photovolt.* **8** 1326–30
[10] Nakada T, Hirabayashi Y, Tokado T, Ohmori D and Mise T 2004 Novel device structure for Cu(In,Ga)Se_2 thin film solar cells using transparent conducting oxide back and front contacts *Sol. Energy* **77** 739–47
[11] Keller J, Chen W-C, Riekehr L, Kubart T, Törndahl T and Edoff M 2018 Bifacial Cu(In, Ga)Se_2 solar cells using hydrogen-doped In_2O_3 films as a transparent back contact *Prog. Photovolt., Res. Appl.* **26** 846–58
[12] Cavallari N *et al* 2017 Low temperature deposition of bifacial CIGS solar cells on Al-doped zinc oxide back contacts *Appl. Surf. Sci.* **412** 52–57
[13] Moon S H, Park S J, Hwang Y J, Lee D-K, Cho Y, Kim D-W and Min B K 2014 Printable, wide band-gap chalcopyrite thin films for power generating window applications *Sci. Rep.* **4** 4408
[14] Zhou C Z, Verlinden P J, Crane R A, Swanson R M and Sinton R A 1997 21.9% efficient silicon bifacial solar cells *Conf. Record of the 26th IEEE Photovoltaic Specialists Conf. (Proc. IEEE)* pp 287–90
[15] Shin M J *et al* 2021 Semitransparent and bifacial ultrathin Cu(In,Ga)Se_2 solar cells via a single-stage process and light-management strategy *Nano Energy* **82** 105729
[16] Yang S-C, Lin T-Y, Ochoa M, Lai H, Kothandaraman R, Fu F, Tiwari A N and Carron R 2023 Efficiency boost of bifacial Cu(In,Ga)Se_2 thin-film solar cells for flexible and tandem applications with silver-assisted low-temperature process *Nat. Energy* **8** 40–51
[17] Deng H , Sun Q, Yang Z, Li W, Yan Q, Zhang C, Zheng Q, Wang X, Lai Y and Cheng S 2021 Novel symmetric bifacial flexible CZTSSe thin film solar cells for indoor photovoltaic applications *Nat. Commun.* **12** 3107
[18] Ahmad F, Civiletti B J, Monk P B and Lakhtakia A 2022 Efficiency enhancement of ultrathin CIGS solar cells by optimal bandgap grading. Part II: new algorithm and double-layer antireflection coatings *Appl. Opt.* **61** 10049–61
[19] Park H K, Cho Y, Kim K, Jeong I, Gwak J, Yun J H and Jo W 2022 Tailored band structure of Cu(In,Ga)Se_2 thin-film heterojunction solar cells: depth profiling of defects and the work function *ACS Appl. Mater. Interfaces* **14** 34697–705
[20] Ahmad F, Lakhtakia A and Monk P B 2021 *Theory of Graded-Bandgap Thin-Film Solar Cells* (Morgan & Claypool)
[21] Berreman D W 1972 Optics in stratified and anisotropic media: 4×4-matrix formulation *J. Opt. Soc. Am.* **62** 502–10
[22] Mackay T G and Lakhtakia A 2020 *The Transfer-Matrix Method in Electromagnetics and Optics* (Morgan & Claypool)
[23] National Renewable Energy Laboratory 2023 Reference solar spectral irradiance: air mass 1.5 (Accessed 6 June 2023) (available at: www.nrel.gov/grid/solar-resource/spectra-am1.5.html)
[24] Nelson J 2003 *The Physics of Solar Cells* (Imperial College Press)
[25] Fonash S J 2010 *Solar Cell Device Physics* 2nd edn (Academic)
[26] Billard J 1966 Contribution a l'Etude de la Propagation des Ondes Electromagnetiques Planes dans Certains Milieux Materiels (2ème these) *PhD Dissertation* vol 6 (Université de Paris) pp 175–8
[27] Mackay T G and Lakhtakia A 2020 *The Transfer-Matrix Method in Electromagnetics and Optics* (Morgan & Claypool)
[28] Dodge M J 1984 Refractive properties of magnesium fluoride *Appl. Opt.* **23** 1980–5
[29] Ehrmann N and Reineke-Koch R 2010 Ellipsometric studies on ZnO:Al thin films: refinement of dispersion theories *Thin Solid Films* **519** 1475–85

[30] Stelling C, Singh C R, Karg M, König T A F, Thelakkat M and Retsch M 2017 Plasmonic nanomeshes: their ambivalent role as transparent electrodes in organic solar cells *Sci. Rep.* **7** 42530
[31] Treharne R E, Seymour-Pierce A, Durose K, Hutchings K, Roncallo S and Lane D 2011 Optical design and fabrication of fully sputtered CdTe/CdS solar cells *J. Phys.: Conf. Ser.* **286** 012038
[32] Minoura S , Maekawa T, Kodera K, Nakane A, Niki S and Fujiwara H 2015 Optical constants of Cu(In,Ga)Se_2 for arbitrary Cu and Ga compositions *J. Appl. Phys.* **117** 195703
[33] Ahmad F *et al* 2018 Optimization of light trapping in ultrathin nonhomogeneous $CuIn_{1-\xi}Ga_{\xi}Se_2$ solar cell backed by 1D periodically corrugated backreflector *Proc. SPIE* **10731** 107310L
[34] Boidin R *et al* 2016 Pulsed laser deposited alumina thin films *Ceramics Int.* **42** 1177–82
[35] Querry M R Defence Technical Information Center 1987 Optical constants of minerals and other materials from the millimeter to the ultraviolet *Contractor Report* CRDEC-CR-88009 (available at: https://apps.dtic.mil/dtic/tr/fulltext/u2/a192210.pdf)
[36] Anderson T H, Civiletti B J, Monk P B and Lakhtakia A 2020 Coupled optoelectronic simulation and optimization of thin-film photovoltaic solar cells *J. Comput. Phys.* **407** 109242
Anderson T H, Civiletti B J, Monk P B and Lakhtakia A 2020 *J. Comput. Phys.* **418** 109561 (erratum)
[37] Sun J and Jasieniak J J 2017 Semi-transparent solar cells *J. Phys. D: Appl. Phys.* **50** 093001
[38] Chatterjee A 2023 Powering internet-of-things from ambient energy: a review *J. Phys. Energy* **5** 022001
[39] Glunz S W, Biro D, Rein S and Warta W 1999 Field-effect passivation of the SiO_2-Si interface *J. Appl. Phys.* **86** 683–91
[40] Dauwe S, Mittelstädt L, Metz A and Hezel R 2002 Experimental evidence of parasitic shunting in silicon nitride rear surface passivated solar cells *Prog. Photovolt., Res. Appl.* **10** 271–8
[41] Bunea G, Wilson K, Meydbray Y, Campbell M and Ceuster D D 2006 Low light performance of mono-crystalline silicon solar cells *4th World Conf. Photovolt. Energy* pp 1312–4
[42] Biswas S and Kim H 2020 Solar cells for indoor applications: progress and development *Polymers* **12** 1338